IOP Publishing Smart Materials and Structures
Smart Mater. Struct. 26 (2017) 095056 (10pp) https://doi.org/10.1088/1361-665X/aa7e66

Self-sensing of dielectric elastomer actuator enhanced by artificial neural network

Zhihang Ye and Zheng Chen

Department of Electrical Engineering and Computer Science Wichita State University, 1845 Fairmount St. Wichita, KS 67260-0083, United States of America

E-mail: zheng.chen@wichita.edu

Received 14 May 2017, revised 30 June 2017
Accepted for publication 7 July 2017
Published 22 August 2017

Abstract

Dielectric elastomer (DE) is a type of soft actuating material, the shape of which can be changed under electrical voltage stimuli. DE materials have promising usage in future's soft actuators and sensors, such as soft robotics, energy harvesters, and wearable sensors. In this paper, a stripe DE actuator with integrated sensing capability is designed, fabricated, and characterized. Since the strip actuator can be approximated as a compliant capacitor, it is possible to detect the actuator's displacement by analyzing the actuator's impedance change. An integrated sensing scheme that adds a high frequency probing signal into actuation signal is developed. Electrical impedance changes in the probing signal are extracted by fast Fourier transform algorithm, and nonlinear data fitting methods involving artificial neural network are implemented to detect the actuator's displacement. A series of experiments show that by improving data processing and analyzing methods, the integrated sensing method can achieve error level of lower than 1%.

Keywords: dielectric elastomer, self-sensing, artificial neural network

(Some figures may appear in colour only in the online journal)

1. Introduction

Many soldiers and civilians lose their hands, arms and legs on battlefields, in accidents, and as the result of natural disasters. Also, many senior people partially or completely lose the functioning of a limb due to the aging process. To help these handicapped people, many researchers have spent years of effort on developing prosthetic or exoskeleton devices to restore limb's functions. Although recent technologies and theories are far from fully simulating the functions of legs and arms [1, 2], the prosthetic research is capturing the attention of researchers. Most research is based on electrical motor-driven prosthetic limbs, varying from a single finger to a full arm [3, 4]. Companies such as DEKA have developed commercial robotic arms controlled by electric motors [5]. For a more compact structure and higher efficiency, many researchers, inspired by biological muscles, used a tendon-driven structure in their designs [6]. Although of this work shows great potential for a bio-inspired design of prosthetic arm or leg, a compliant actuator is still missing.

In order to overcome the limits of an electrical motor, many researchers turn to investigate the feasibility of using smart materials in traditional applications. Dielectric elastomer (DE) is a kind of important electro active polymer, which has unique combination of flexibility, light weight, high energy density, and direct generation of movement [7]. A typical DE actuator is usually made into membrane shape with two compliant electrodes coated on both sides, then it can be stretched, stacked, or rolled into multiple configurations [8]. When voltage (higher than 1000 V) is applied to the electrodes, the Maxwell stress between the two electrodes will compress the elastomer membrane in the direction of electrical field [8]. Pelrine studied DE actuators and electro-magnetics in terms of energy density (energy per unit mass). He reported that DE material has an energy density that is about eight times greater than that of electro-magnetics, and is also capable of performing more than 100% strain [7, 9–12]. Many studies have also shown that with DE artificial muscles, artificial limbs are capable of generating enough force for humans' daily usage [9, 13].

In existing researches on DE material, many of them are focusing on the modeling, and control of the actuator in applications [8, 13–16]. Moreover, due to the actuator's capacitive structure, a number of researchers attempt to study

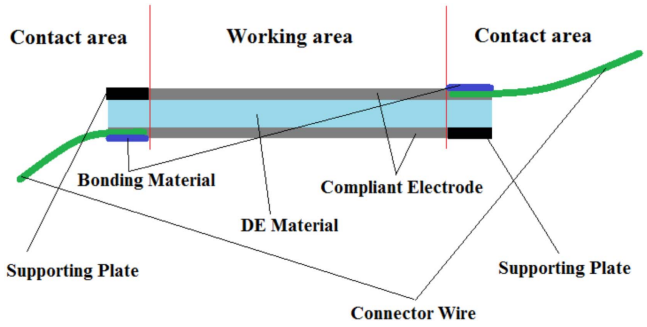

Figure 1. Design of bio-inspired artificial muscle.

the actuators' integrated sensing capabilities and their realization in applications [17–20]. Most of the reported approaches are focused on the analysis of the actuators' impedance changes during the displacement period. The existing methods usually require additional component in the circuit loop, such as serial or parallel connected resistance, or a DE actuator with special structure. The integrated sensing function is practiced in the output feedback control of the DE actuator, however, due to the noise of the capacitive reading and the drift of the capacitance-strain rate, it is challenging to achieve satisfactory control performance [21].

In this paper, a DE artificial muscle with integrated sensing and actuation is developed. Inspired by biological muscle, this DE artificial muscle has the similar shape and movement generating style as natural muscle. In addition, its electrical impedance changes as its voltage-driven strain changes, which leads to integrated sensing of the actuator. By doing this, it is possible to detect the actuator's displacement without using external sensors. The proposed method does not require additional circuit component, or specially designed actuator structure, which will reduce the need for additional hardware, relating impact on actuator performance, and give more freedom to the usage of self-sensing function. The designed method to perform integrated sensing function is to add a probing signal to the actuator's base driving voltage. The actuator's driving voltage is a low frequency signal with large magnitude, in the contrast, the probing signal has high frequency and small magnitude. By adjusting the probing signal's frequency to a proper value, the probing signal can be well separated from the base driving voltage. System identification also shows that the actuator plays as an low-pass filter which can minimize the probing signal's impact on the actuation result. The effect of probing frequency on integrated sensing has been investigated and an optimal probing frequency has been found out based on the experimental data. Fast Fourier transform (FFT) is used to extracted the probing signal, and artificial neural network (ANN) tool is introduced to analyze the changes probing signal. Experimental results show that ANN can handle this nonlinear data fitting task well, and ANN based estimation makes the integrated sensing method more robustness to sensing noise, and disturbance in applications.

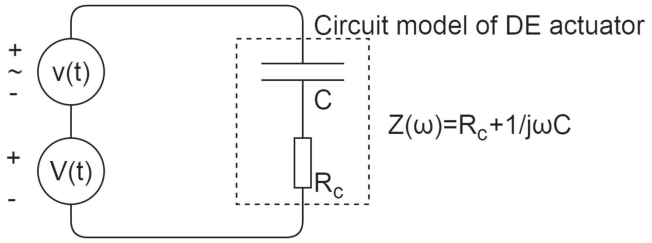

Figure 2. Mechanism of integrated sensing.

The rest of the paper is organized as follows: design and fabrication of the actuator is shown in section 2. Experimental results are discussed in section 3. Section 4 shows how to improve the accuracy of displacement prediction with ANN network. Conclusions and future work are discussed in section 5.

2. Design and fabrication of bio-inspired artificial muscle

A cross-sectional view of the actuator design is shown in figure 1. The actuator presents a typical sandwiched structure with two compliant electrodes. A variety of conductive materials, including carbon particle, carbon grease, metal powder, can be used in the fabrication of compliant electrode. 3M VHB tape, cured polymer material, and other sticky material, which can join the strip and connector together, and sustain displacement strain is a candidate for the bonding material. On the other side of bonding material's area, a rigid plate is attached to maintain the actuator's strip shape.

A 3M VHB 4905 tape strip of 15 $\times$ 7.5 cm size was cut from a tape roll. The strip was stretched in the longitudinal direction by 100%, and fixed on a holding frame. Two wood plates of 10 $\times$ 1 cm size were attached on the middle edge of the stretched tape. The edges of the tape strip were covered with insulating material to avoid short circuit between two electrode. Then graphite powder (Hillman Inc.) was pasted uniformly on both sides of the tape strip. After the electrodes were well established, the actuator was cut off from the tape strip. Since weight load was attached on the wood plate which were fixed to the vertical edges of DE membrane, vertical prestretch was caused by the attached weight load, which is nearly 150% with a 100 g load. The device's size was nearly 9.4 $\times$ 10 cm, and the elliptical shape in the middle was due to the one-directional pre-stretching before cutting off from the original strip.

When the strip generated a movement, its length increase led to a higher surface resistance, and its compressed thickness resulted in a higher capacitance. Hence, the actuator's displacement caused the impedance change of the actuator, and this change could reflect the displacement of the actuator. Figure 2 is showing the mechanism of the proposed integrated sensing function.

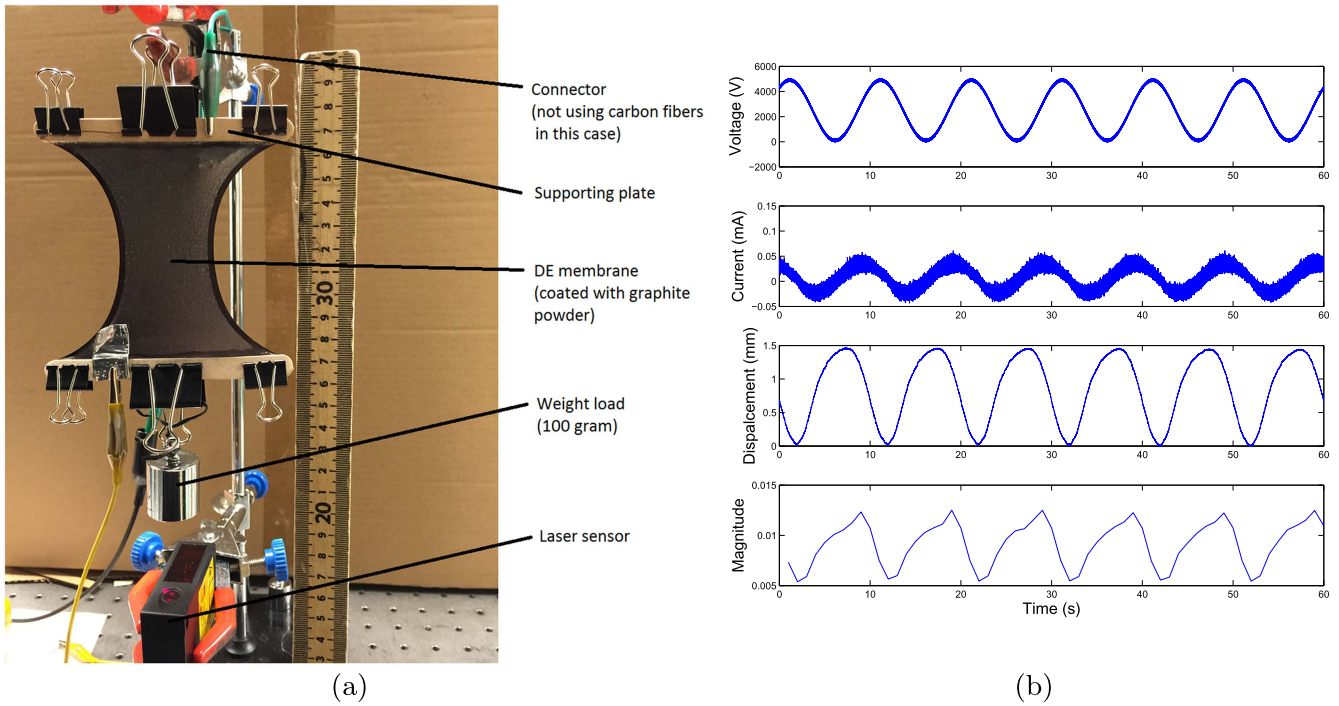

Figure 3. The first test of self-sensing capability: (a) experimental setup; (b) experimental result.

3. Experimental results

3.1. Actuation dynamics

The weight load's position was controlled by the applied voltage. The high voltage caused Maxwell stress between the two electrodes, and led to compression effect in the VHB tape's thickness direction. This compression made the tape strip expand in its planar directions, then the weight load was lowered down. In the first test, the actuation voltage was a sinusoidal wave of 100–4900 V range and 0.1 Hz frequency. The probing signal was also a sinusoidal wave, whose amplitude and frequency were set as 100 V and 50 Hz, respectively. The actuator has a capacitor structure, which means AC input will go through the actuator. An AC input with very high frequency may cause excessive load on the power supply, and large amplitude may damage the membrane. As shown in the figure 3(a), one end of the actuator was fixed to a metal frame. A calibration weight of 100 g was attached to the other end of the actuator, and the weight load was allowed to move vertically. The two electrodes were connected to a high voltage amplifier (5HVA24-BP1-F, UltraVolt Inc.), which was controlled by a dSPACE (DS1104, dSPACE Inc.) control board. A displacement laser sensor (Baumer OADM 20I6441/S14F) was placed under the weight load to capture load movements. Here an actuation voltage was set between 100 and 4900 V, and a sinusoidal wave with a magnitude of 100 V and high frequency (50–100 Hz) was added to the actuation voltage. Both voltage and current were measured by a dSPACE's real-time control system. The sampling rate of the dSPACE's ADC unit was set to 1 kHz. Figure 3(b) shows the experimental results, where the first row of the figure was the total input voltage given to the actuator. The second row is the measured current response, the third row showed the displacement measured by the laser sensor, and the last row was the magnitude of probing signal's current extracted during the experiment. From figure 3(b), one can see that there existed a relationship between the actuator's displacement and the magnitude of probing signal's current.

In order to evaluate the impact of high frequency probing signal in the actuator's actuation performance, an empirical method was used to find a transfer function, which could approximate the actuation dynamics of the actuator. In order to measure the actuator's frequency responses, driving voltages (100–4900 V) with different frequencies were given to the actuator, where the full voltage input range (0–5000 V) was normalized between 0 and 1. Then the magnitude of the actuator's response was measured (in mm unit), and was calculated in dB unit. A frequency response of the actuator without probing signal was collected, and a third-order transfer function with a cut-off frequency of 10.5 rad s^{-1} was used to approximate it, which is shown in figure 4(a). Then in the following step, a sinusoidal signal with 100 V amplitude and 50 Hz frequency was added to the input channel. Similarly, a third-order transfer function was used to approximate the response points, which was showing in figure 4(b). By comparing figures 4(a) and (b), one can conclude that the frequency responses with and without probing signal are very close and the probing signal does not impact the actuation response significantly. The transfer function for approximation of the actuator is shown as

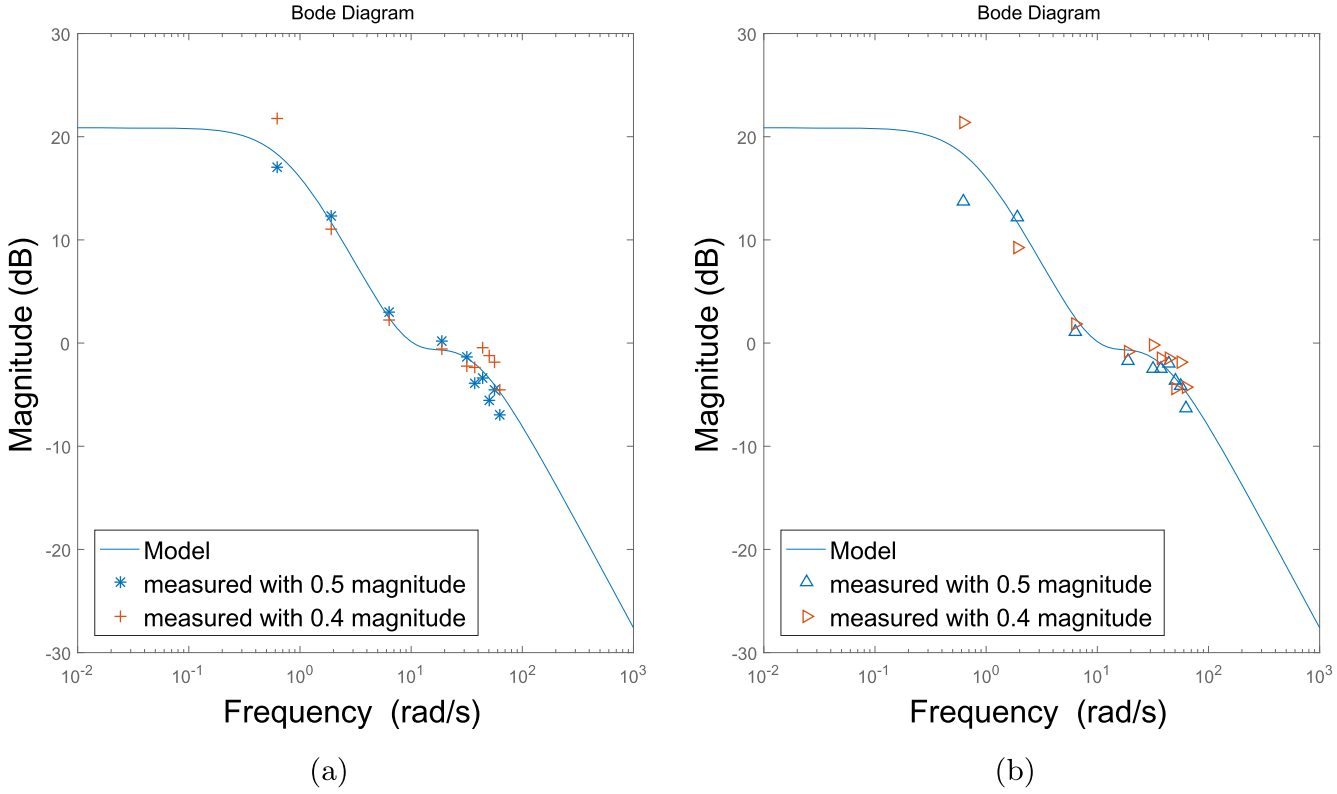

Figure 4. (a) Model without probing signal; (b) model with probing signal added.

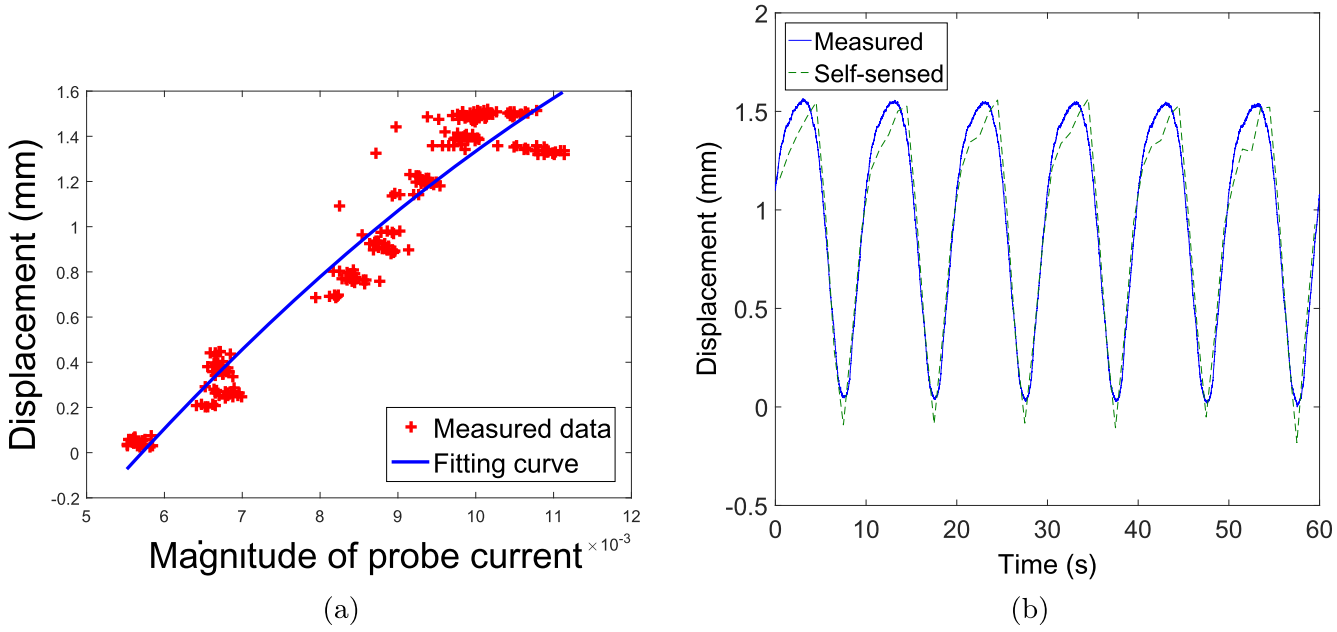

Figure 5. (a) Second-order polynomial fitting curve of 50 Hz probing signal; (b) comparison of measured displacement and self-sensed displacement with polynomial fitting.

following equation:

$$G(s) = \frac{0.09537s^2 + 1.681s + 11.05}{0.002286s^3 + 0.1159s^2 + 1.509s + 1}. \quad (1)$$

The probing signal's frequency should be higher than 21 rad s^{-1}, which was two times of the actuator's cut-off frequency.

3.2. Integrated sensing with polynomial curve-fitting method

Polynomial curve fitting is a useful tool to obtain the mapping relationship. Based on former experimental settings, data over a continuous 4 min was collected. A polynomial curve-fitting function was extracted form this 4 min of data. Another one minute of data was collected with the same experimental setup and used to verify the mapping function that was

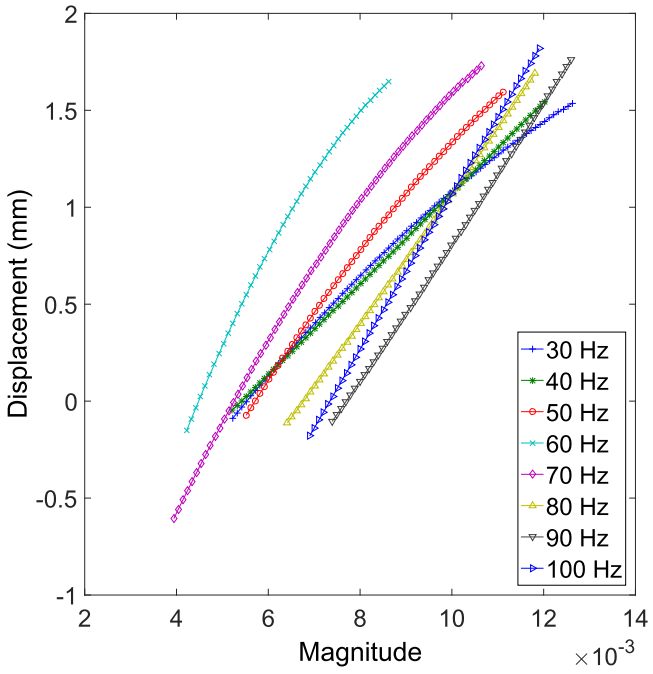

Figure 6. Comparison of fitting curves.

obtained from former experiments. Figure 5(a) shows a second-order polynomial curve-fitting result of the 4 min of data. The measured and estimated displacements are plotted in figure 5(b).

To investigate the impact of probing frequency on the self-sensing performance, a series of probing signals with the same magnitude but different frequencies (30–100 Hz, in 10 Hz steps) were tested in experiments. The fitting curves are plotted in figure 6. These fitting curves with different probing frequencies have some differences, but the average estimation errors are similar. Table 1 shows the average error with different probing frequencies. Some data sets had an unusually high error level, which was probably due to some issues (disturbance, noise) occurring during the data collection process. But other data sets also had a close error level. Hence, the probing frequency does not have a significant effect on the self-sensing accuracy. In order to minimize power consumption, the probing frequency should be as low as possible. But it is also very important to keep the frequency of sensing signal higher than a reasonable value to separate it from the driving signal. From table 1, one can conclude that 50 Hz was the best probing frequency in terms of both low estimation error and low power consumption.

4. Self-sensing with ANN

In order to reduce the estimation error of the self-sensing, an ANN was employed to estimate the displacement output based on the magnitude of probing current signal. ANN is a powerful tool for nonlinear fitting. An ANN consists of one or several layers of artificial neurons. In a typical three-layer ANN, the first layer is referred to as the input layer, a hidden layer connects the input layer, and the last layer is called the output layer. Neurons in the hidden layer are connected to neurons in the first and last layers. Each neuron has its weight, bias, and transfer function, and with the help of training data and a specific training algorithm, all neurons are changing their weight and bias values to achieve the nonlinear fitting goal [22].

ANN is a computational model which can handle multiple tasks such as classification, nonlinear mapping, pattern recognition [23–25]. An ANN consists a numbers of simple units which are called artificial neuron, figure 7(a) is showing a scheme of artificial neuron, where function $\phi(.)$ is the neurons transfer function. An artificial neuron has a bias a, input $\vec{x}$, and each of the input has a weight coefficient w respectively. With the inputs and bias, the artificial neurons output y can be calculated as following equation:

$$y(\vec{x}) = \phi\left(\sum_{l=1}^{n}(x_l w_l + a)\right). \tag{2}$$

In a typical layered ANN, the network contains n input sites in its input layer, k neurons in the hidden layer, and m neurons in its output layer, figure 7(b) is showing the structure of a layered ANN. An artificial neuron in the input layer is connected to each neuron in the hidden layer, and the neurons in the hidden layer have individual bias. Here treats the bias in hidden layer neurons as a weighted input of value 1, so the weight from for ith input layer neuron to jth hidden layer neuron is $w_{ij}^{(1)}$. Then the weight matrix between input layer and hidden layer is W_1, which is a $n + 1$ by k matrix. Similarly, the weight matrix between hidden layer and output layer is W_2, which is a $k + 1$ by m matrix.

The ANN must be trained with training data before using in a specific task. A training data set is required for training, which contains vector(s) with correct input and output values as its elements. For example, the ith training vector $z_i = [\vec{o}, \vec{t}]$, where $\vec{o}$ is the input vector and $\vec{t}$ is the target vector. Back-propagation (BP) algorithm is a widely used method to train an ANN. The main steps of BP algorithm including 3 steps: feed-forward computation, BP to layers, and weight updates.

Take the former layered ANN as an example, in feed-forward step, the input values of a training vector o are input into the ANN, and the inputs of each layer after input layer are obtained through the neurons mathematical equations. Here uses $o^{(1)}$ for the outputs of hidden layer, and $o^{(2)}$ for the outputs of output layer.

Then the BP step is done in the reversed direction. First the quadratic error of output layer E is computed as equation:

$$E = \sum_{j=1}^{m}\frac{1}{2}(o_j^{(2)} - t_j^2)^2. \tag{3}$$

The algorithm wants to find the weight $w_{ij}^{(2)}$ which can minimize the error E, Then the partial derivatives $\frac{\partial E}{\partial w_{ij}^{(2)}}$ is needed. By defining the multiplicative terms $\delta_j^{(2)}$ as:

$$\delta_j^{(2)} = o_j^{(2)}(1 - o_j^{(2)})(o_j^{(2)} - t_j). \tag{4}$$

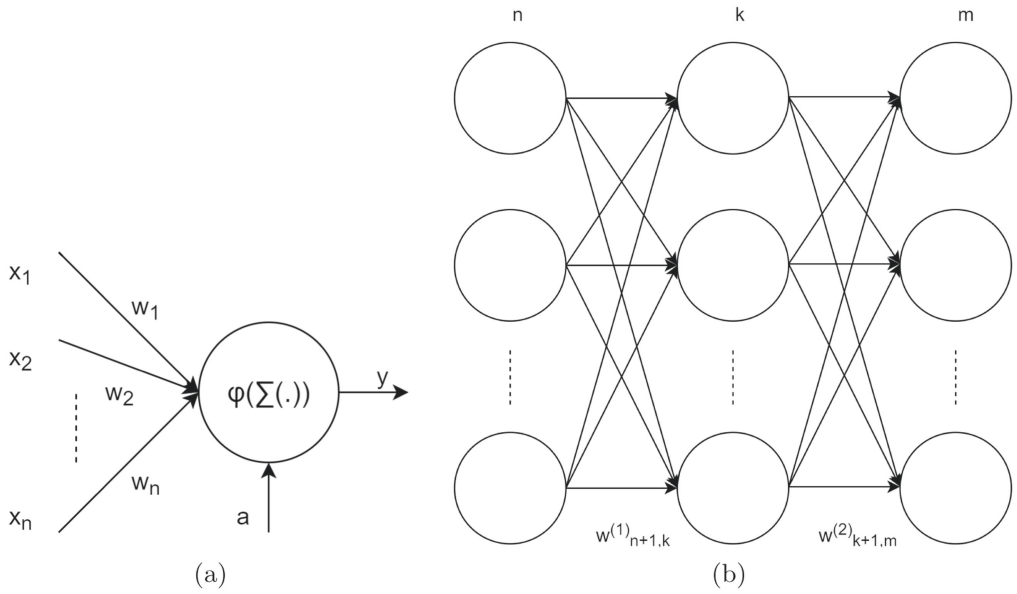

Figure 7. (a) A schematic view of artificial neuron; (b) structure of a layered artificial neural network.

Table 1. Integrated sensing error of different probing frequencies.

Probing frequency (Hz)	30	40	50	60	70	80	90	100
Error (%)	7.77	7.31	6.43	8.44	10.63	7.30	7.65	9.12

One can get the partial derivative as:

$$\frac{\partial E}{\partial w_{ij}^{(2)}} = o_i^{(1)} \delta_j^{(2)}. \tag{5}$$

Now use chain rule to get the partial derivatives for hidden layer, since each neuron in hidden layer is connected to the neurons in output layer, the BP error can be calculated as:

$$\delta_j^{(1)} = o_j^{(1)}(1 - o_j^{(1)}) \sum_{l=1}^{m} w_{ij}^{(2)} \delta_l^{(2)}, \tag{6}$$

where $w_{il}^{(2)}$ is the weight form jth hidden layer neuron to lth output layer neuron. And the wanted partial derivatives $\frac{\partial E}{\partial w_{ij}^{(1)}}$ can be obtained as:

$$\frac{\partial E}{\partial w_{ij}^{(1)}} = o_i \delta_j^{(1)}. \tag{7}$$

Now the weights for each layer can be updated in the negative gradient direction. Set a small learning rate α, then the weights can be updated as:

$$w_{ij}^{(2)} = w_{ij}^{(2)} + \Delta w_{ij}^{(2)} = w_{ij}^{(2)} - \alpha o_i^{(1)} \delta_j^{(2)}, \tag{8}$$

$$w_{ij}^{(1)} = w_{ij}^{(1)} + \Delta w_{ij}^{(1)} = w_{ij}^{(1)} - \alpha o_i \delta_j^{(1)}. \tag{9}$$

If a training data set contains p vectors, then the update directions are calculated for each vector, and the final gradient direction is:

$$\Delta w_{ij}^{(1)} = \Delta_{(1)} w_{ij}^{(1)} + \Delta_{(2)} w_{ij}^{(1)} + ... + \Delta_{(p)} w_{ij}^{(1)}. \tag{10}$$

4.1. Fitting results with ANN

In this subsection, two types of ANN, normal ANN and enhanced ANN, were employed for estimating the displacement output. Same data sets were used again for training the ANNs to fit the curve between the measured magnitude and the displacement. In the first test, a two-layer BP neural network, which is a normal ANN, was built and trained by 4 min of data. Then another one minute of data was used to verify the network. Figure 8(a) shows the fitting curve done by the neural network, and figure 8(b) shows the displacement curve, the sensed value of displacement peak were not very ideal, but the overall error level was much better than polynomial curve fitting. With the neural network, the error level was 2.74%, less than half of the former fitting result. Probing signals with different frequencies were also tested with neural network. In addition to some data sets being largely affected by noise or disturbance, all data sets showed a decreasing error level. Figure 9(a) shows the fitting curves of all frequencies, and the average error level is shown in table 2.

In order to obtain more accurate and robust self-sensing results, an enhanced ANN with additional data-handling methods were used in following calculation: first, the FFT window was changed. In the former tests, each FFT window contained 1000 data points and was separated, which means 60 data could only give 60 data points. For more data points from a data set of the same length, a rolling window was employed during data extraction. The length of the FFT window was still 1000 points, but each time the window was

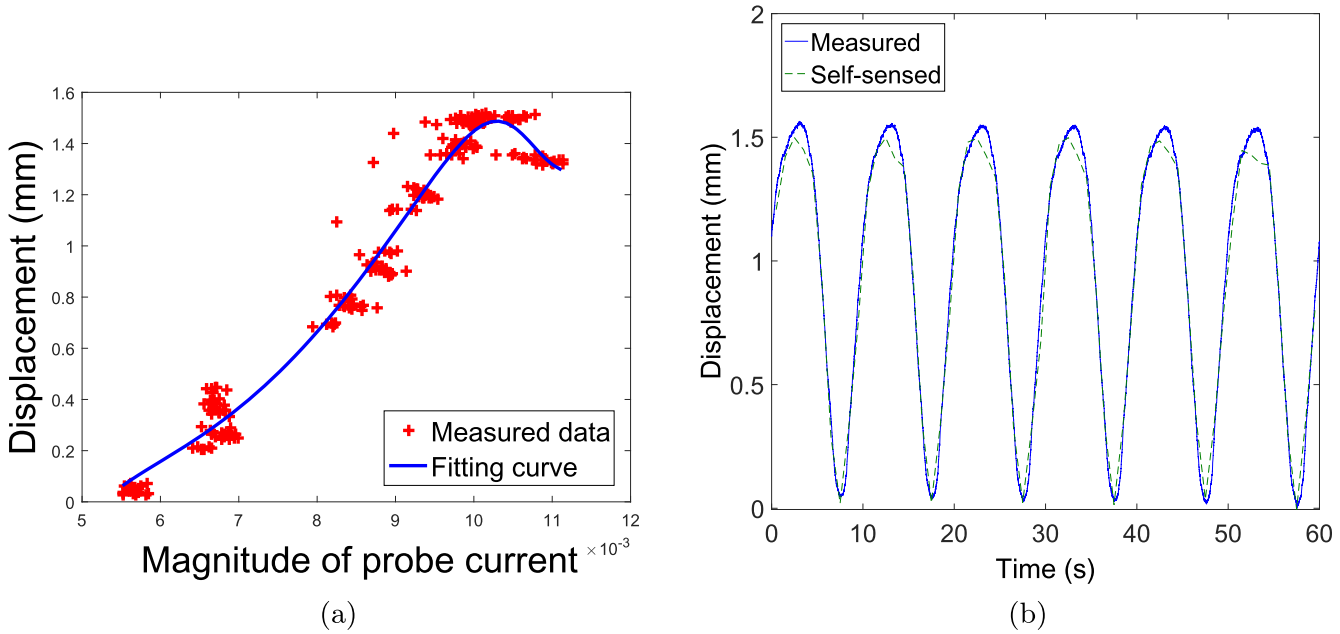

Figure 8. (a) Neural network fitting curve of 50 Hz probing signal; (b) comparison of measured displacement and self-sensed displacement with ANN fitting.

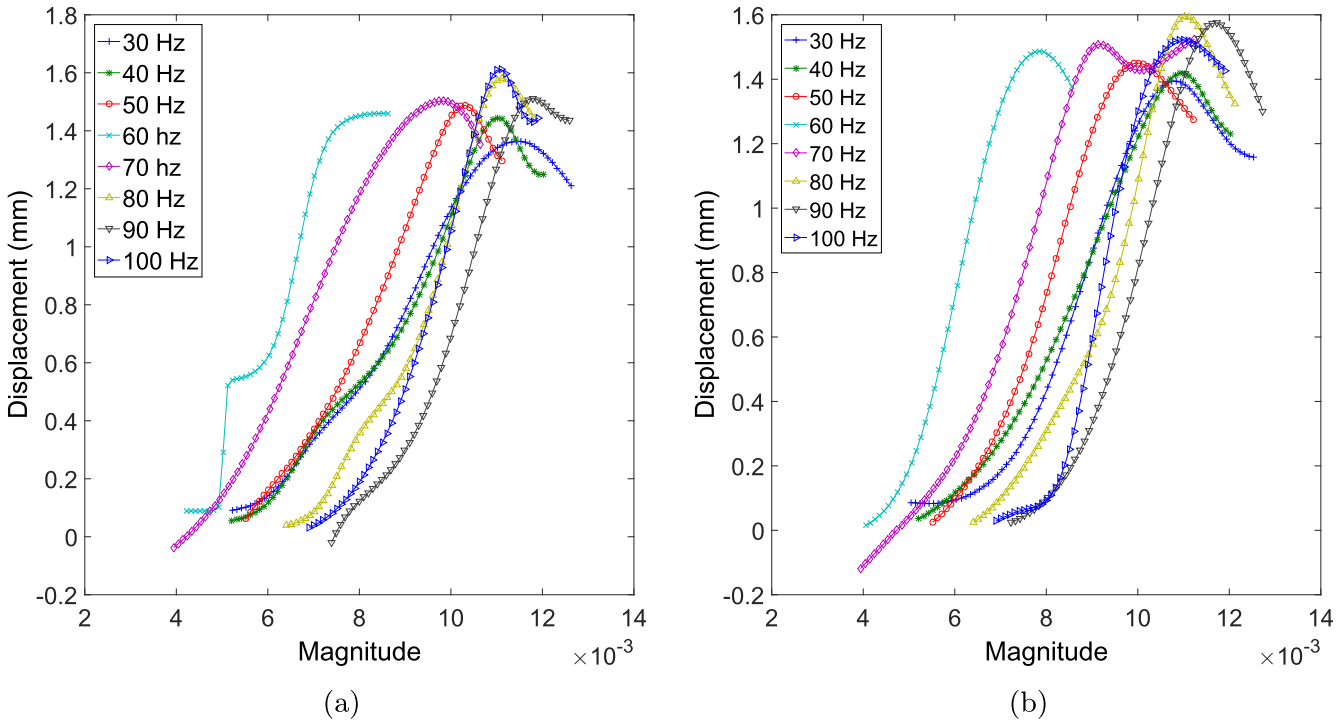

Figure 9. (a) Comparison of ANN fitting curves. (b) Comparison of enhanced ANN fitting curves.

Table 2. ANN integrated sensing error of different probing frequencies.

Probing Frequency (Hz)	30	40	50	60	70	80	90	100
Error of normal ANN (%)	4.67	3.13	2.74	6.31	11.54	4.56	6.90	4.80
Error of enhanced ANN (%)	4.18	2.32	2.62	3.25	5.30	2.48	2.72	4.75

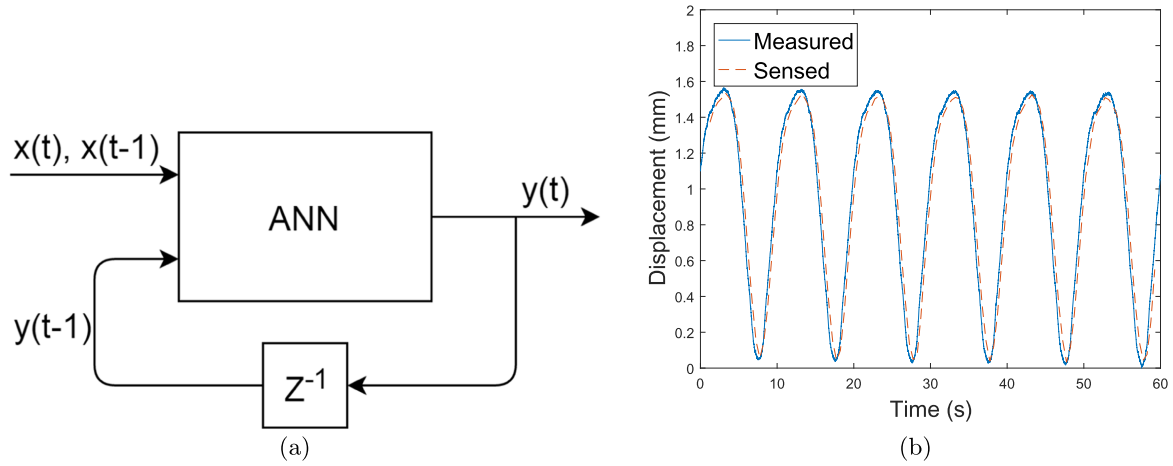

Figure 10. (a) Input output structure of proposed NARX network; (b) detection result of NARX network with 50 Hz probing signal.

moved 500 points forward, the number of data point was doubled. Second, the input of the neural network did not have only one value but rather included one current magnitude value and one latest historical magnitude value. In this way, the neural network could discern the trend of the device's displacement. The neural network had four neurons in this case, and worked with at least two magnitude-displacement data points. The fitting results of the 50 Hz probing signal has an average error level of 2.62% (compared to 2.74%); therefore, for well-collected data, these additional data processing methods would not give obvious enhancement of the fitting accuracy. But when it came to heavily compromised data, such as data with a 70 Hz probing signal, the average error was diminished by nearly half of its former level. The error was 11.54% before, and in this case it was only 5.30%. In summary, the overall fitting results with extra processing methods are shown in figure 9(b). By comparing these results with the former fitting results, it can be seen that the pattern of each fitting curve is more unified, which means that the fitting result is more robust than previously. In table 2, the accuracy improvement of compromised data is also apparent.

4.2. Integrated sensing using nonlinear auto-regressive network with exogenous input

Nonlinear auto-regressive network with exogenous input (NARX) is widely used in prediction of time series, such as economic behavior, chemical process and identification of dynamic systems [26, 27]. In an NARX network, a system's output time series $y(t)$ is considered as a function of the past values of the time series, and a second time series $x(t)$:

$$y(t) = f(y(t-1), y(t-2), \ldots, y(t-p), \\ x(t-1), x(t-2), \ldots, x(t-p)), \quad (11)$$

where $y(t-p)$ is the system's output at sampling time $t-p$, and $x(t-p)$ is the system's input at sampling time $t-p$. Specifically, in this integrated sensing case, the system's sensing result $y(t)$ is supposed to satisfy following equation:

$$y(t) = f(y(t-1), x(t), x(t-1)), \quad (12)$$

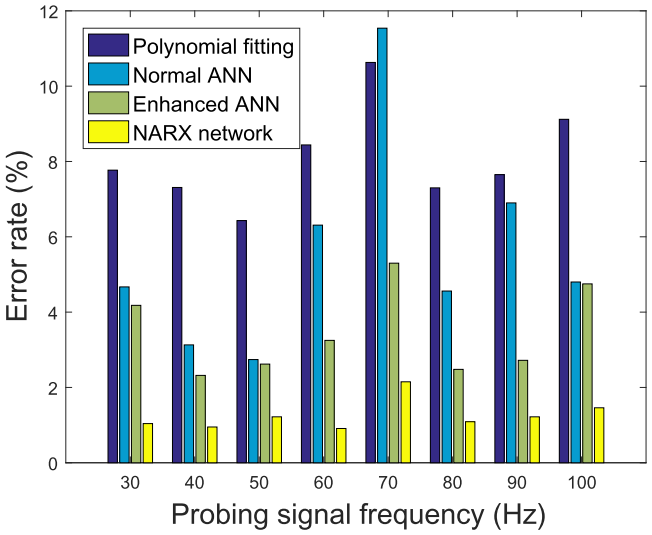

Figure 11. Comparison of all fitting methods.

where $y(t-1)$ is the system's previous output, $x(t-1)$ is the previous input, and $x(t)$ is the newest extracted magnitude of probing signal. Hence, the new ANN's input output structure is showing in figure 10(a). This NARX network has 3 input terminals, 7 artificial neurons in hidden layer, and 1 neuron in output layer. Before input data into this ANN, the same data pre-processing method for enhanced ANN prediction is used here. The fitting result based on 50 Hz probing signal is showing in figure 10(b), one can see that the predicted curve fits the actual curve well, since this NARX network method can well address the nonlinearity of the actuator's displacement in the peak range. For a clear view of the improvement, the error level of all fitting methods are shown in figure 11.

Since NARX network has better fitting accuracy in this case, more simulations were practiced to find out the impact of network's parameters on the fitting result. Based on the former NARX network, where input was sinusoidal wave with 100–4900 V magnitude and 0.1 Hz frequency, and

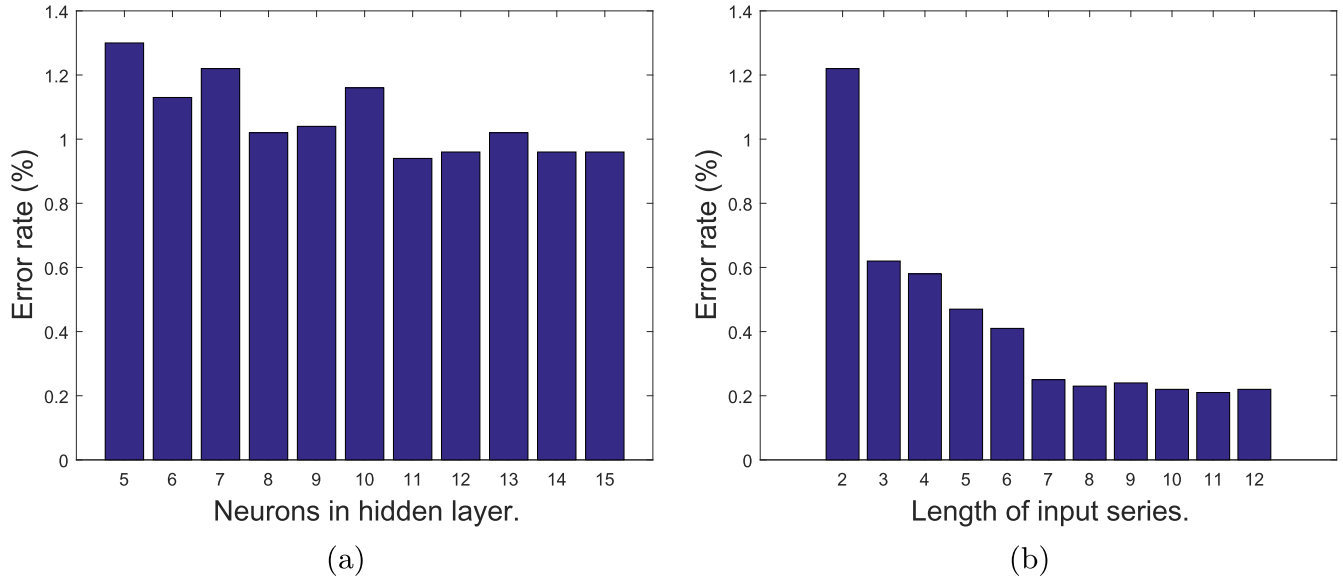

Figure 12. (a) Fitting error level with different hidden layer size; (b) detection error rates with different lengths of input series.

probing signal was sinusoidal wave of 100 amplitude and 50 Hz frequency. The size of hidden layer was changed from 5 to 15 neurons, and the fitting error is shown in figure 12(a). From the figure one can see too small or too large hidden layer size are not helpful for a better fitting result, only set the hidden later with a proper size will give good fitting accuracy. Since the complexity of the network did not increase too much in this simulation, all the training steps are finished in 3 s. The effect of input series' length was also tested with a NARX network of 7 hidden neurons, and the same input and probing signal. By changing the input time series' length from 2 to 10, the corresponding error levels are shown in figure 12(b). One can see that longer input series generally gives better fitting result, but that also requires more computation resource, longer training time, and longer initial time for the network to output detection result. It is recommended to make a proper trade off between fitting accuracy and resources requirements.

5. Conclusions and future work

In this paper, a strip DE actuator with integrated sensing and actuation capability has been developed, whose actuation and integrated sensing capabilities have been characterized. An integrated sensing method has been performed with the consideration of the actuator's high frequency impedance changes. Experimental results have shown that the integrated sensing mechanism can be simultaneously performed when the actuator is generating displacement. With the help of integrated sensing function, the actuator's displacement can be detected without using of external sensors. Further results show that the software method has significant impact on the detection accuracy. Second-order polynomial fitting, normal ANN, enhanced ANN and NARX network have been used to estimate the displacement, of which the NARX network achieved the lowest error level (less than 1%).

In the future's work, one important part is to improve the accuracy of integrated sensing function. In addition, how the shape of the DE actuators affect the integrated result is also an interesting aspect. Since a proper data processing method has significant impact on the sensing accuracy, developing advanced data processing method is another important research direction. The application of integrated sensing in feedback control is the most fascinating goal in the future's research.

Acknowledgments

This research was supported in part by the National Science Foundation under CAREER Grant DCSD #1653301 and Multidisciplinary Research Project Award (MURPA) Wichita State University.

ORCID iDs

Zheng Chen https://orcid.org/0000-0002-5339-7596

References

[1] Bogue R 2009 Exoskeletons and robotic prosthetics: a review of recent developments *Ind. Robot: Int. J.* **36** 421–7
[2] Lai J, Schoen M, Gracia A P, Naidu D and Leung S 2007 Prosthetic devices: challenges and implications of robotic implants and biological interfaces *Proc. Inst. Mech. Eng.* H **221** 173–83
[3] Massa B, Roccella S, Carrozza M C and Dario P 2002 Design and development of an underactuated prosthetic hand *IEEE Int. Conf. on Robotics and Automation, 2002. Proc. ICRA'02* vol 4 (IEEE) pp 3374–9

[4] Rouse E J, Mooney L M, Martinez-Villalpando E C and Herr H M 2013 Clutchable series-elastic actuator: design of a robotic knee prosthesis for minimum energy consumption *2013 IEEE Int. Conf. on Rehabilitation Robotics (ICORR)* (IEEE) pp 1–6
[5] DEKA, The deka arm www.dekaresearch.comùdeka_arm.shtml.
[6] Li Q M and Li Y W 2014 Anthropomorphic optimization of a rope-driven prosthetic finger *Appl. Mech. Mater.* **568** 899–903
[7] Pelrine R, Kornbluh R, Joseph J, Heydt R, Pei Q and Chiba S 2000 High-field deformation of elastomeric dielectrics for actuators *Mater. Sci. Eng.* C **11** 89–100
[8] Suo Z 2010 Theory of dielectric elastomers *Acta Mech. Solida Sin.* **23** 549–78
[9] Pelrine R, Kornbluh R, Pei Q and Joseph J 2000 High-speed electrically actuated elastomers with strain greater than 100% *Science* **287** 836–9
[10] Pelrine R, Sommer-Larsen P, Kornbluh R D, Heydt R, Kofod G, Pei Q and Gravesen P 2001 Applications of dielectric elastomer actuators *Proc. SPIE* **4329** 335–49
[11] Plante J-S 2006 Dielectric elastomer actuators for binary robotics and mechatronics *PhD Thesis* Massachusetts Institute of Technology
[12] Plante J-S, Devita L M and Dubowsky S 2007 A road to practical dielectric elastomer actuators based robotics and mechatronics: discrete actuation *Proc. SPIE* **6524** 652406
[13] Carpi F, De Rossi D, Kornbluh R, Pelrine R E and Sommer-Larsen P 2011 *Dielectric Elastomers as Electromechanical Transducers: Fundamentals, Materials, Devices, Models and Applications of an Emerging Electroactive Polymer Technology* (Amsterdam: Elsevier)
[14] Liu L, Liu Y and Leng J 2013 Theory progress and applications of dielectric elastomers *Int. J. Smart Nano Mater.* **4** 199–209
[15] Brochu P and Pei Q 2010 Advances in dielectric elastomers for actuators and artificial muscles *Macromol. Rapid Commun.* **31** 10–36
[16] Carpi F and De Rossi D 2007 Contractile folded dielectric elastomer actuators *Proc. SPIE* **6524** 65240D
[17] O'Brien B, Thode J, Anderson I, Calius E, Haemmerle E and Xie S 2007 Integrated extension sensor based on resistance and voltage measurement for a dielectric elastomer *Proc. SPIE* **6524** 652415
[18] Jung K, Kim K J and Choi H R 2008 A self-sensing dielectric elastomer actuator *Sensors Actuators* A **143** 343–51
[19] Chuc N H, Thuy D V, Park J, Kim D, Koo J, Lee Y, Nam J-D and Choi H R 2008 A dielectric elastomer actuator with self-sensing capability *Proc. SPIE* **6927** 69270V
[20] Gisby T A, O'Brien B M and Anderson I A 2013 Self sensing feedback for dielectric elastomer actuators *Appl. Phys. Lett.* **102** 193703
[21] Rosset S, OBrien B M, Gisby T, Xu D, Shea H R and Anderson I A 2013 Self-sensing dielectric elastomer actuators in closed-loop operation *Smart Mater. Struct.* **22** 104018
[22] Rojas R 2013 *Neural Networks: A Systematic Introduction* (Berlin/Heidelberg, Germany: Springer Science & Business Media)
[23] Haykin S and Network N 2004 A comprehensive foundation *Neural Netw.* **2** 41
[24] Rowley H A, Baluja S and Kanade T 1998 Neural network-based face detection *IEEE Trans. Pattern Anal. Mach. Intell.* **20** 23–38
[25] Demuth H B, Beale M H, De Jess O and Hagan M T 2014 *Neural Network Design* (Stillwater, OK: Martin Hagan)
[26] Diaconescu E 2008 The use of narx neural networks to predict chaotic time series *Wseas Trans. Comput. Res.* **3** 182–91
[27] Menezes J M P and Barreto G A 2008 Long-term time series prediction with the narx network: an empirical evaluation *Neurocomputing* **71** 3335–43